12th International Symposium on Turbulence and Shear Flow Phenomena (TSFP12)
Osaka, Japan, July 19–22, 2022

DYNAMICS OF SECONDARY MOTIONS IN TURBULENT CHANNELS WITH STREAMWISE RIDGES

K. Schäfer, B. Frohnapfel, D. Gatti

Institute of Fluid Mechanics,
Karlsruhe Institute of Technology,
Karlsruhe, Germany
kay.schaefer / bettina.frohnapfel / davide.gatti@kit.edu

ABSTRACT

The present study investigates secondary motions in turbulent open-channel flow with streamwise-aligned ridges by direct numerical simulations. The large domain size chosen for this study allows the presence of very-large-scale motions (VLSM) for smooth wall conditions. The spanwise spacing of the ridges S is systematically varied to investigate its influence on the interaction of secondary motions and VLSM, as well as their coexistence. In the recent experiments by Zampiron *et al.* (2020) no contribution of VLSM is found for dense ridge spacings $S \leq \delta$, where δ is the half-channel height, while for wide ridge spacings VLSM and secondary motion can coexist. However, the spectra reveals a contribution of VLSM for $S = 2\delta$, which corresponds to the spanwise wavelength of naturally occuring VLSM and was not observed in the experiments, suggesting that coexistence of secondary motions and VLSM might be possible for this ridge spacing.

INTRODUCTION

Many technical and environmental flows occur over spatially heterogeneous surfaces, while smooth surfaces tend to be the exceptions. In particular, heterogeneous surfaces that vary in the direction normal to the mean flow can cause the emergence of so-called turbulent secondary motion. These are streamwise-aligned counter-rotating vortices and can significantly alter the momentum and heat transport of the turbulent flow (Stroh *et al.*, 2020). Secondary motions were found over various heterogeneous surface types, such as streamwise-aligned ridges (Vanderwel *et al.*, 2019; Zampiron *et al.*, 2020) or alternating rough and smooth wall strips (Wangsawijaya *et al.*, 2020; Schäfer *et al.*, 2022). It has been found, for instance, that the characteristic spanwise wavelength or distance of the surface inhomogeneity influences the spatial extent of the secondary motion in the time-spatial mean (Wangsawijaya *et al.*, 2020; Zampiron *et al.*, 2020). For wavelengths of many times the outer length scale of the flow (the thickness of a turbulent boundary layer, for instance), the flow splits into regions affected by the secondary motions (e.g., at the smooth-rough transition or close to the ridges) and homogeneous flow regions not influenced by the wall inhomogeneity. If the wavelength is of the order of the boundary layer thickness, the secondary motion is the strongest (Wangsawijaya *et al.*, 2020). A further reduction of the spacing leads to a reduction of the spatial extent of the secondary motions which scales with the spanwise distance S.

While many of the previous studies have investigated secondary motions in a time-averaged sense, a few recent studies focused on the time-dependent properties of secondary motions, which might be masked by the averaging procedure (Vanderwel *et al.*, 2019; Zampiron *et al.*, 2020; Wangsawijaya *et al.*, 2020). To these characteristics belong, that high and low momentum regions found in turbulent secondary motions appear to meander in a manner similar to large-scale motion (LSM) and very-large-scale motions (VLSM) found in high-Reynolds-number flows above smooth walls (Zampiron *et al.*, 2020). Additionally, secondary motions and LSM/VLSM are characterized by large-scale roll circulation in the instantaneous flow field, however the flow structures of the secondary motions are spanwise locked at the surface transition and time-persistent (Wangsawijaya & Hutchins, 2022). The reason of the spatial meandering of the secondary motions remains unclear as well as the dynamical characteristics of their instantaneous flow structures.

In the present study we aim to contribute to a better understanding of these characteristics by performing direct numerical simulations of turbulent open-channel flow with streamwise-aligned ridges. The wide aspect ratio of the adopted open-channel domain allows the occurrence of meandering of the VLSM. The spanwise spacing of the ridges is varied, such that the different flow regimes found in the experiments by Zampiron *et al.* (2020) are reproduced and extended to larger spacings. The temporally and spatially highly resolved data provide an excellent basis to better investigate the spatial and dynamical properties of the instantaneous flow structures associated with secondary motions. In addition, to study the influence of these flow structures on the heat transfer, an additional passive scalar is considered in the simulations.

METHODOLOGY

The direct numerical simulation of the fully developed turbulent open-channel flow is driven at a constant pressure gradient (CPG) corresponding to the effective friction Reynolds numbers $\mathrm{Re}_{\tau,eff.} = 540$, based upon the friction velocity u_τ, the domain height $\delta_{eff.}$ and the kinematic viscosity ν. The effective domain height $\delta_{eff.}$ takes into account the presence of the Gaussian ridges, which reduces the cross-sectional area of the channel. In addition, a temperature transport equation is solved, representing a passive scalar with Prandtl number $Pr = 1$. The simulation domain is $L_x \times L_y \times L_z = 36\delta \times \delta \times 12\delta$ and the number of grid points for discretiza-

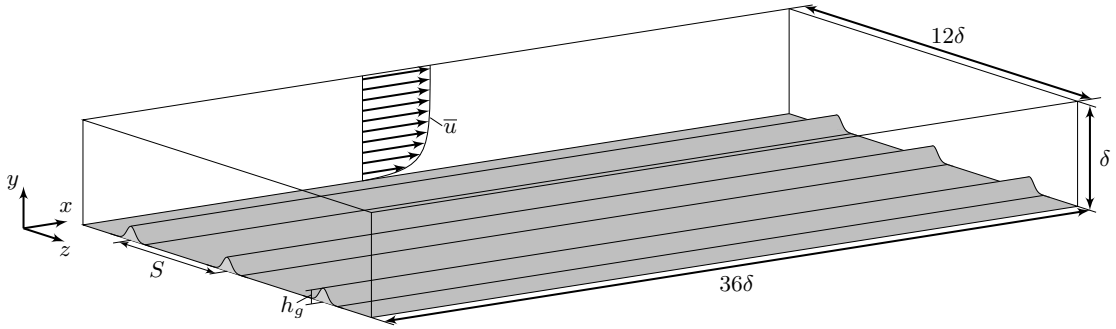

Figure 1. Schematic of open-channel flow domain with streamwise aligned Gaussian ridges.

tion is $N_x \times N_y \times N_z = 3072 \times 257 \times 1152$. In the wall-parallel directions periodic boundary conditions are applied, while no-slip boundary conditions are imposed at the bottom wall and symmetry boundary conditions on the top wall. Streamwise-aligned Gaussian ridges are placed on the wall of the channel, as depicted in Figure 1, with a fixed ridge height $h_g = 0.1\delta$. Three different spanwise spacings S of the Gaussian ridges are explored with $S/\delta = 1, 2, 4$. At the bottom wall, a constant temperature is applied and at the top of the domain a zero-flux condition. In order to avoid a constant heating of the flow volume and to reach a stationary state of the temperate field a source term is added to the temperature transport equation.

The incompressible Navier-Stokes equations are solved with the open source code Xcompact3d (Bartholomew *et al.*, 2020). Sixth-order compact finite difference schemes are used for the spatial discretization and time integration is performed with a third-order Runge-Kutta method. The representation of the Gaussian ridges is achieved by an immersed boundary method (IBM) based on a high order polynomial reconstruction method to guarantee a smooth solution between fluid and solid region (Gautier *et al.*, 2014).

The velocity and temperature field is split by means of a triple decomposition into:

$$u_i(x,y,z,t) = \langle \overline{u}_i \rangle(y) + \tilde{u}_i(y,z) + u_i''(x,y,z,t) \quad (1)$$
$$= \langle \overline{u}_i \rangle(y) + u_i'(x,y,z,t) \quad (2)$$

where $\langle \overline{u}_i \rangle$ is the temporal, streamwise and spanwise averaged velocity, $\tilde{u}_i$ is the coherent component, which is the spatial fluctuation in z about $\langle \overline{u}_i \rangle$, and u_i'' is the random fluctuation. The sum of coherent component and random fluctuation results in the turbulent fluctuation u_i'. Streamwise and temporal averages are indicated by $\overline{\cdot}$ and spanwise averaging by angular brackets $\langle \cdot \rangle$.

RESULTS

The introduction of streamwise aligned ridges in a turbulent channel leads to the formation of secondary motions. Since the simulations are run at constant pressure gradient, the introduction of Gaussian ridges leads to a decrease in bulk velocity u_b^+ (superscript $+$ represents viscous units) and consequently to a reduced bulk Reynolds number $Re_b = u_b \delta_{eff}/\nu$ and an increased friction coefficient $C_f = 2u_\tau^2/u_b^2$. Secondary motions introduce a spanwise inhomogeneity of the mean flow, as can be seen for the present Gaussian ridges in figure 2. The upward motion of the secondary motion is centered at the ridge position for all rough cases. For the largest spanwise ridge spacings $S/\delta = 2, 4, 12$ the secondary motion have their largest spanwise extent, while for $S/\delta = 0.5$ and 1 the spanwise and vertical extent of the secondary motion cell is reduced, which scales with S. The smooth wall case still displays some upward bulging of the mean streamwise velocity at specific spanwise positions, e.g. $z/\delta \approx 2.5$, which is the statistical footprint of the slow dynamics of VLSM, which appear due to the limited time integration for two-dimensional statistics. For the specific case $S/\delta = 4$ an additional upward bulging of the mean streamwise velocity can be observed in the center between adjacent ridges. A similar spatial inhomogeneity is also found for the mean temperature field for all ridge cases, resulting in higher temperature values which extend into the bulk region above the ridges (not shown here).

Table 1. Global flow properties of simulation cases.

$\mathrm{Re}_{\tau,eff.}$	S/δ	Re_b	u_b^+	$C_f(\cdot 10^{-3})$	Nu
540	∞	9845	18.22	6.03	15.05
540	12	9786	18.13	6.08	15.11
540	4	9612	17.80	6.32	15.31
540	2	9411	17.45	6.57	15.51
540	1	9233	17.11	6.83	15.85
540	0.5	9098	16.84	7.05	16.84

The instantaneous flow structures, such as low- and high-momentum regions, present for the smooth and ridge cases are shown in figure 3 for the instantaneous streamwise velocity fluctuations u' in the horizontal plane at the wall-normal position $y = 0.5\delta$. For the smooth wall case $S/\delta = \infty$ the spatial meandering of the VLSM can be observed by long streamwise coherent low- and high-velocity streaks, e.g. at $z/\delta \approx 10$ a high-momentum region is found with a streamwise wavelength $\lambda_x \approx 20\delta$. For the largest ridge spacing $S = 12\delta$ a strong and streamwise coherent low-speed streak is found at the spanwise position of the ridge, while at some spanwise distance of the ridge the spatial meandering of the high-speed streaks of VLSM are visible again. The strength of the low-speed streak at the ridge is amplified compared to the ones found for smooth wall conditions, which is also the case for $S = 4\delta$. For $S = 4\delta$ less intense low-speed streaks with some streamwise coherence can be observed between adjacent ridges. At denser ridge spacing $S = 2\delta$ and $S = \delta$ the low-speed streaks are also located in correspondence with the ridges and are pronounced, however their streamwise extent is interrupted. The same is even more evident for denser ridge spacings. Finally, for the densest ridge spacing $S = 0.5\delta$ the streamwise coherence of

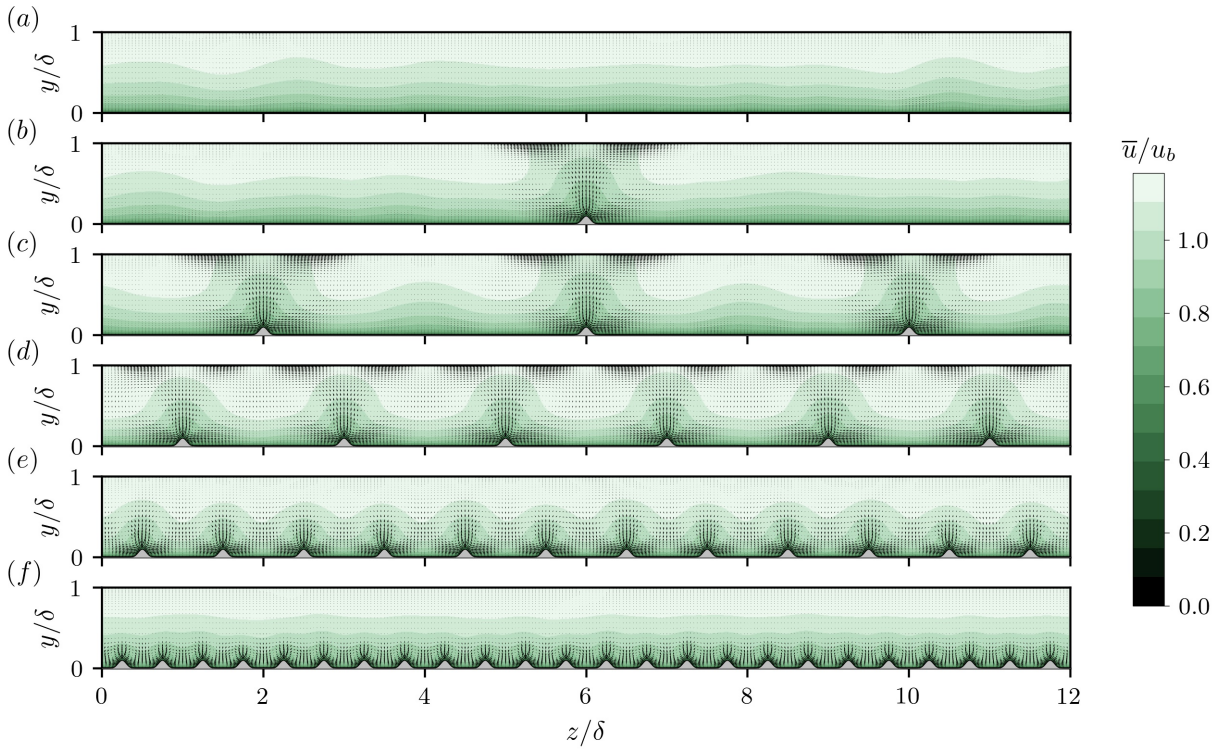

Figure 2. Mean streamwise velocity in y-z cross section: (a) smooth wall; (b) $S = 12\delta$; (c) $S = 4\delta$; (d) $S = 2\delta$; (e) $S = \delta$; (f) $S = 0.5\delta$.

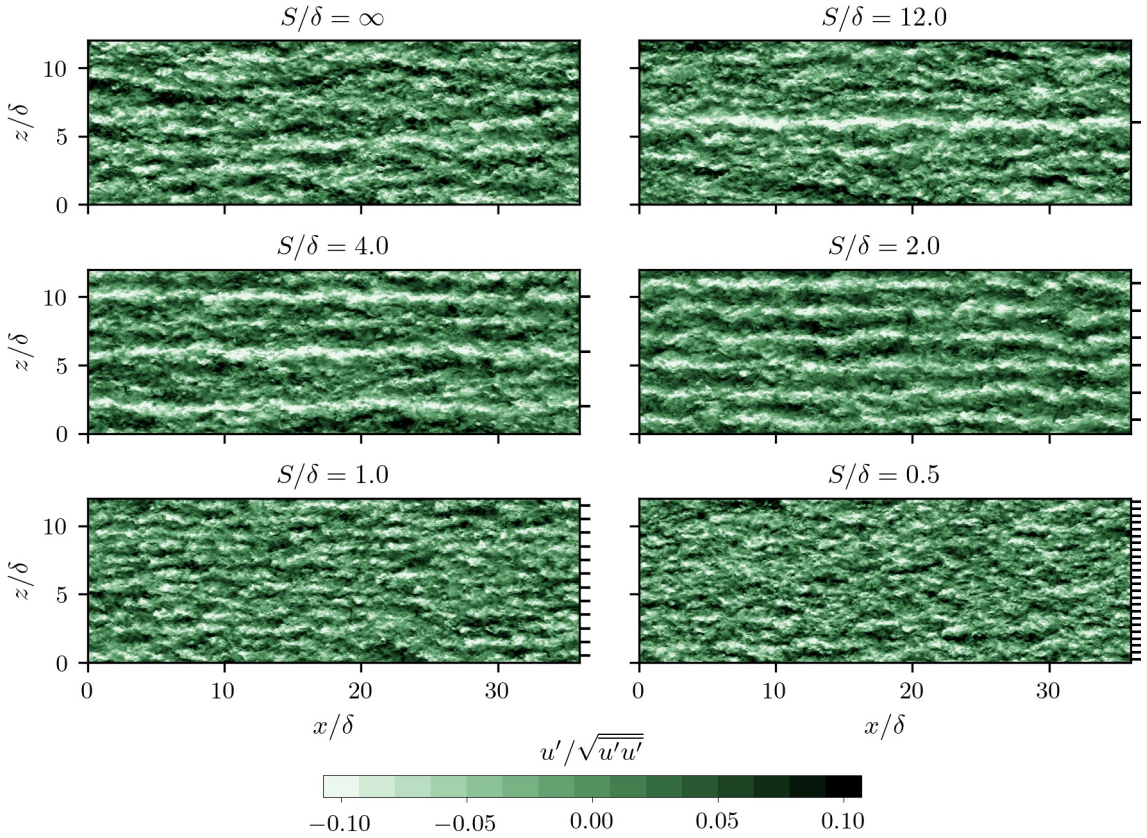

Figure 3. Instantaneous streamwise velocity fluctuations in horizontal plane at $y = 0.5\delta$ for smooth wall case $S/\delta = \infty$ and different spanwise ridge spacings S. The black horizontal lines at the outer right figure frame indicate the spanwise position of the ridges.

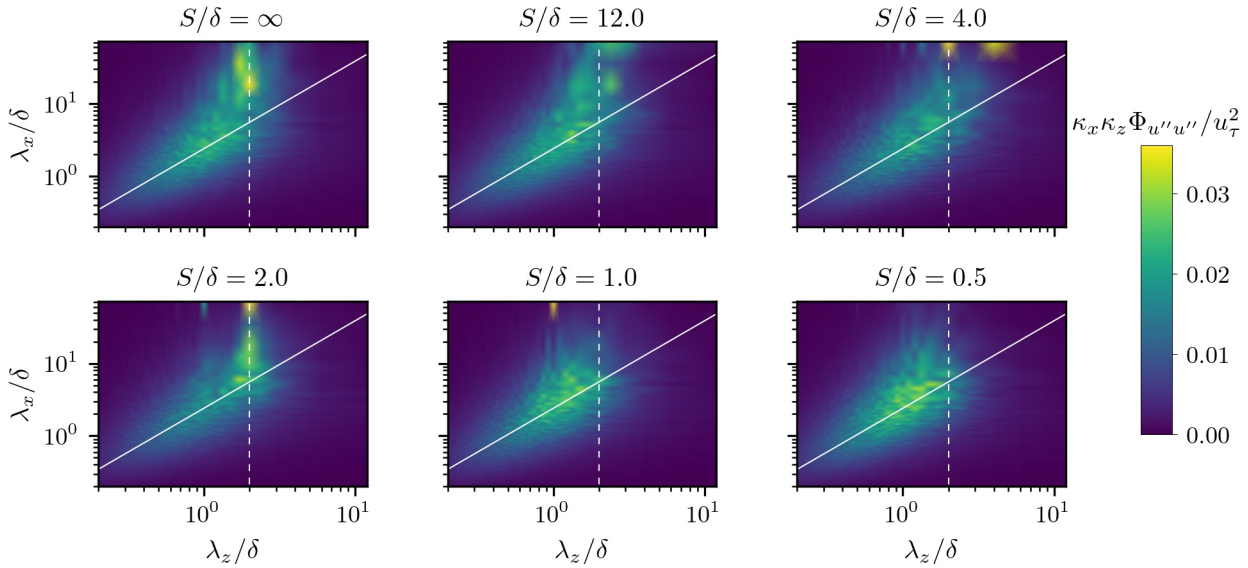

Figure 4. Pre-multiplied two-dimensional streamwise energy spectra $\kappa_x\kappa_z\Phi_{u''u''}$ as a function of the streamwise wavelength λ_x and spanwise wavelength λ_z at $y = 0.5\delta$ for smooth wall case $S/\delta = \infty$ and ridge cases.

the low-speed streaks is broken and the spanwise ridge position cannot be inferred anymore. Comparison of the streamwise velocity fluctuations with the temperature fluctuations T' reveal a strong correlation between both fields and the position and spatial extent of the low-speed streaks coincides with intense values of T' (not shown here).

The contribution of the meandering VLSM and low- and high-velocity streaks in the instantaneous snapshots can be quantified by the two-dimensional power spectral density of the streamwise turbulent fluctuations $\Phi_{u''u''}$ in the streamwise and spanwise direction, which is defined as

$$\langle\overline{u''u''}\rangle(y) = \int_0^\infty \int_0^\infty \Phi_{u''u''}(\kappa_x, y, \kappa_z)\,\mathrm{d}\kappa_x\,\mathrm{d}\kappa_z, \qquad (3)$$

where the streamwise and spanwise wavenumber are defined as $\kappa_x \equiv 2\pi/\lambda_x$ and $\kappa_z \equiv 2\pi/\lambda_z$ and λ_x and λ_z are the streamwise and spanwise wavelength. Figure 4 presents the energy spectra at the wall-normal position $y = 0.5\delta$ for the smooth wall case and ridge cases. Note that the energy concentration of the streamwise mean (contribution of $\kappa_x = 0$) has been artificially placed at the streamwise wavelength $\lambda_x = 72$ to present the contribution of stationary and non-meandering structures. The inclined gray line indicates that an increase of streamwise wavelength λ_x of the flow structures goes in hand with an increase of the spanwise wavelength λ_z up to $\lambda_z \approx 2\delta$.

The VLSM for the smooth wall case show a clear concentration of energy in the range of $\lambda_z \approx 2\delta$ (indicated by the dashed gray line) with two strong and distinct peaks at $\lambda_x = 18\delta$ and $\lambda_x = 36\delta$. The coarsest ridge case $S = 12\delta$ also displays high energy concentration for $\lambda_x = 18\delta$, where one peak appears at slightly larger λ_z compared to the smooth wall case. These strong peaks for large λ_x cannot be found for $S = 4\delta$, however high values are now concentrated in the stationary component of the mean streamwise energy for wavelength $\lambda_z = 2$ and $\lambda_z = 4$, which corresponds to the spanwise wavelengths of the low-speed streaks observed in figure 3 of $S = 4\delta$. This illustrates that VLSM cannot strongly meander for $S = 4\delta$ as it is the case for the smooth wall case and $S = 12\delta$. Interestingly, the meandering behaviour of VLSM at $\lambda_x \approx 18$ reappears for $S = 2\delta$ together with some contribution of the mean streamwise energy at the same spanwise wavelength. For the denser ridge spacings $S = \delta$ and $S = 0.5\delta$ this energy contribution for large λ_x cannot be found anymore, which is consistent with the experimental observations of Zampiron *et al.* (2020). This indicates that a spanwise ridge spacing which is in the range of spanwise wavelength of the natural occurring VLSM allows spatial meandering of large-scale motion, while this is inhibited for $S = 4\delta$ and not present for denser ridge spacings. For $S = 2\delta$ an additional energy peak for smaller streamwise wavelengths $\lambda_x \approx 6\delta$ and $\lambda_z \approx 1.8\delta$ can be found, which also appears for denser ridge spacings in a similar λ_z range.

To illustrate at which spanwise position the large-scale motions occur, figure 5 shows the one-dimensional energy spectrum $\kappa_x\Phi_{u''u''}$ across the spanwise coordinate z at two different wall-normal positions $y = 0.25\delta$ and $y = 0.5\delta$. The smooth wall case $S = \infty$ depicts large values for $\lambda_x \geq 10\delta$ at all spanwise position with some strong peaks due to slow dynamics of VLSM. Case $S = 12\delta$ in contrast, shows a clear separation of the energy for large λ_x, where no energy contribution is found at the spanwise position of the ridge, while high energy similar to the smooth wall case is found in the wide smooth wall region unaffected by the secondary motions. However, high energy contributions are found for $\lambda_x \leq 10\delta$ at the spanwise position of the ridge. The energy deficit of large λ_x at the ridges is also observed for $S = 4\delta$ at $y = 0.25\delta$ and partially at $y = 0.5\delta$, where for instance large-scale contributions are found on both lateral sides of the ridge at $z = 2\delta$. Interestingly, high energy contributions are also found in the middle between two ridges at $y = 0.5\delta$ for all λ_x, which depict similar values as the contribution at the ridges. For case $S = 2\delta$ stronger energy peaks between $3\delta \leq \lambda_x \leq 10\delta$ occur at the ridges. Unlike the coarse ridge spacings, energy contributions from high λ_x now appear constantly at the ridges, while in the valleys no contributions is present. The main contribution of streamwise energy of case $S = \delta$ is in the range of intermediate λ_x, while contributions of large λ_x are less frequent.

The one-dimensional energy spectrum $\kappa_z\Phi_{u''u''}$ across the wall-normal coordinate y is shown figure 6 (a). The general shape of the energy spectrum is similar among the smooth wall and ridge cases. The smooth wall case features an additional high energy contribution at $\lambda_z \approx 1.8\delta$, which is not visible for

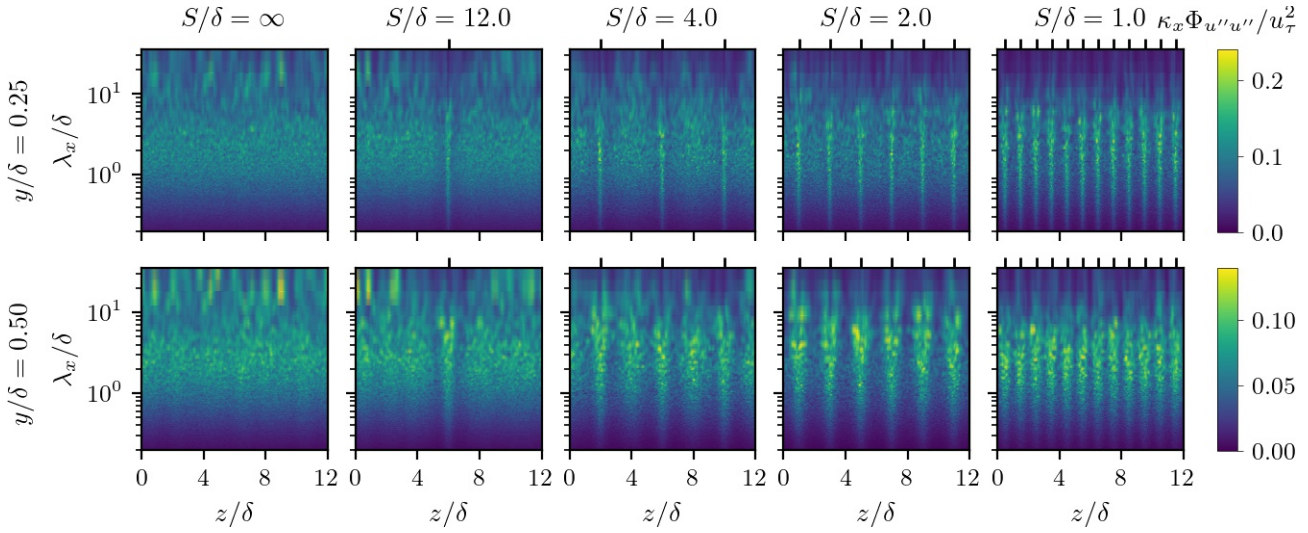

Figure 5. Pre-multiplied streamwise energy spectra $\kappa_x \Phi_{u''u''}$ as a function of the streamwise wavelength λ_x and spanwise position z at two wall-normal positions: top panel $y/\delta = 0.25$ and bottom panel $y/\delta = 0.5$. The spanwise position of the ridges is indicated by the vertical lines at the outer top figure frame.

$S = 12\delta$, $S = 4\delta$ and $S \leq \delta$. For $S = 2\delta$ a high energy contributions reappears in a similar range of λ_z, which extends to higher wall-normal positions. As shown in the streamwise energy spectra in figure 4 and 5 at $y = 0.5\delta$ this contribution at $\lambda_z \approx 2$ is related to flow structures with large streamwise wavelengths λ_x. To further illustrate the contribution of these very-large scale structures across the wall-normal height the streamwise energy spectrum $\kappa_z \Phi_{u''u''}$ is integrated only for structures with $\lambda_x \geq 10\delta$ and presented in figure 6 (b). As can be seen for the smooth wall case the additional peak in figure 6 (a) is due to the contribution of the large-scale streamwise structures ($\lambda_x \geq 10\delta$) with $\delta \leq \lambda_z \leq 2.2\delta$, which have high energy contributions up to $y = 0.7\delta$. The range of the energy contribution is similar for the coarse ridge spacing case $S = 12\delta$, which features lower maximum values and with decreasing ridge spacing S the contribution area shrinks. Finally for the small ridge spacings $S \leq \delta$ no contributions of very-large scales is found.

The energy contribution of the time- and streamwise-averaged secondary motions in figure 2, which do not meander in the streamwise direction, is not reflected in the energy contribution of $u''u''$. Similar to the energy spectrum of the streamwise random fluctuation $\Phi_{u''u''}$, the one-dimensional power spectral density of the streamwise coherent component $\Phi_{\tilde{u}\tilde{u}}$ is defined as

$$\langle \tilde{u}\tilde{u} \rangle (y) = \int_0^\infty \Phi_{\tilde{u}\tilde{u}}(y, \kappa_z) \, \mathrm{d}\kappa_z, \tag{4}$$

which represents the energy contribution of the stationary secondary motions shown in figure 6 (c) (Wangsawijaya & Hutchins, 2022). The energy spectrum $\Phi_{\tilde{u}\tilde{u}}$ does not show any contribution for the smooth wall case, since no coherent motion is present in the time- and streamwise-averaged velocity field. The coherent contribution for case $S = 12\delta$ is weak, because large parts of the spanwise domain are unaffected by the secondary motions appearing at the single ridge. Interestingly, for case $S = 4\delta$ an energy contribution of the coherent velocity appears at $\lambda_z \approx 2.3\delta$ instead of $\lambda_z \approx 4\delta$ corresponding to the spanwise spacing of the ridges. This is related to the appearance of the additional upward bulging between the ridges seen in figure 2. This energy contributions for $\lambda_z \approx 2.3\delta$ is intensified for case $S = 2\delta$ showing a peak region at $y \approx 0.45\delta$, overlapping with the contribution of large streamwise wavelengths of the fluctuating random velocity contribution. In addition, sub-harmonics with smaller wall-normal extent appear. For $S = \delta$ the contributions at $\lambda_z \approx 2.3$ vanish and the primary energy contributions of the stationary secondary motions is concentrated at $\lambda_z \approx \delta$. In addition, the wall-normal extent of this peak is reduced compared to $S = 2\delta$, which is consistent with the reduced spatial bulging of the secondary motions for small values of S in figure 2.

CONCLUSION & OUTLOOK

The present study investigates secondary motions in turbulent open-channel flow with streamwise aligned ridges. The spanwise spacing of the ridges S is varied to study its influence on the interaction of secondary motions and very-large-scale motions and their coexistence. The recent experimental study of Zampiron *et al.* (2020) suggest that VLSM cannot coexist with ridge-induced secondary motions for ridge spacings $S \lessapprox 2\delta$, but can coexist for wider ridge spacing as shown for $S \approx 4\delta$. In agreement with these experimental findings, the present DNS reveal the appearance of VLSM for wide ridge spacing $S = 12\delta$ in the broad smooth wall region between the ridge-induced secondary motion. They meander similarly to the VLSMs in the smooth channel. However, for $S = 4\delta$ we observe for the present case that the spectral signature of VLSM is weakened compared to the smooth wall and ridge case $S = 12\delta$, and for this case the VLSM are not able to strongly meander. This observation might be related to the smaller Reynolds number used for the simulations compared to the experiments, since VLSM intensify with increasing Reynolds number (Hutchins & Marusic, 2007), and thereby might surpass the influence of secondary motions. While VLSM are weaker for $S = 4\delta$, the velocity spectrum shows stronger contribution of turbulent structures in the center between the ridges for a similar range as for the secondary motion with $\delta \leq \lambda_x \leq 10\delta$. This suggests that for $S = 4\delta$ turbulent structures are also preferentially located between the ridges, which contributes to an additional upward bulging of the mean velocity in this region, which is however weaker than the secondary motion (compare with figure 2).

Also in line with the experimental results no contribution

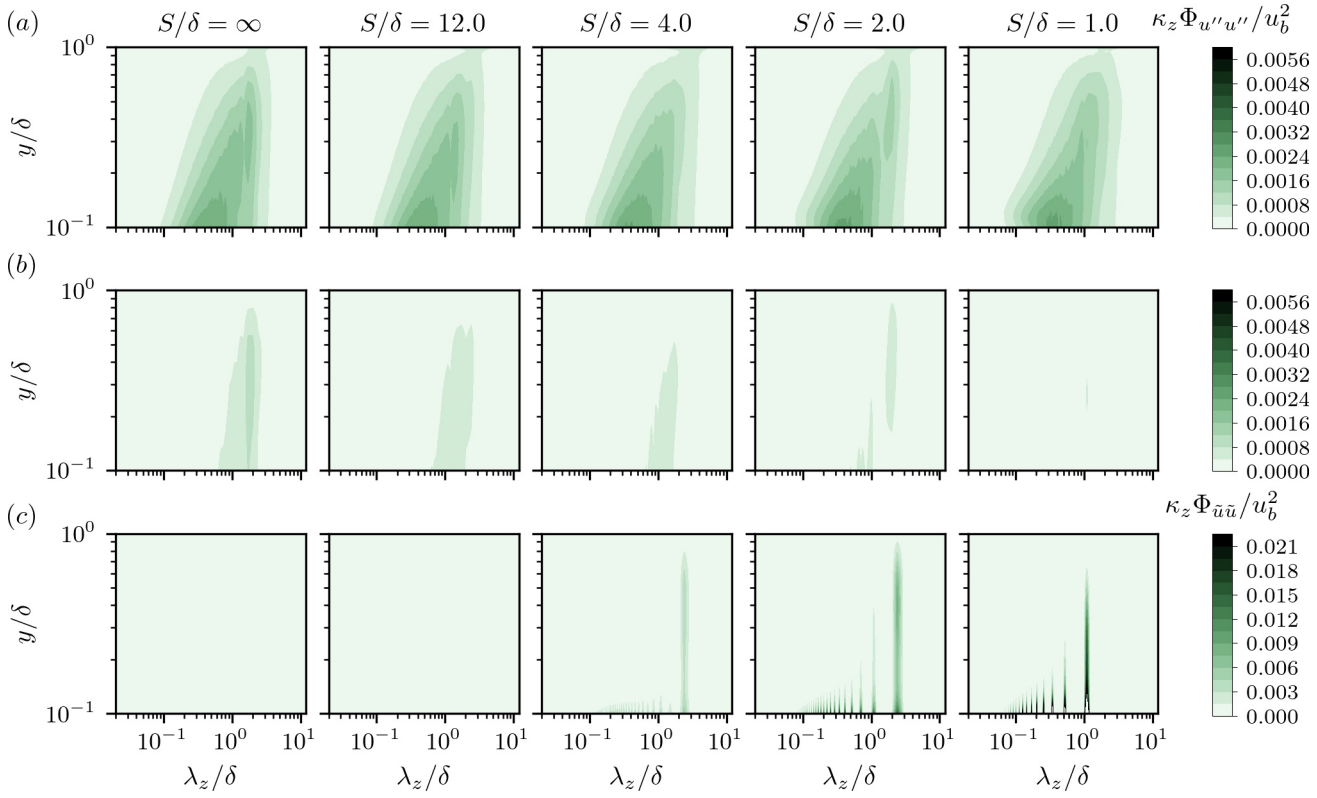

Figure 6. Pre-multiplied streamwise energy spectra $\kappa_z\Phi_{u''u''}$ as a function of the wall-normal position y and spanwise wavelength λ_z for all streamwise wavelengths λ_x in (a) and only for $\lambda_x \geq 10\delta$ in (b). The pre-multiplied energy spectra of the coherent streamwise velocity $\kappa_z\Phi_{\tilde{u}\tilde{u}}$ is shown in (c).

of VLSM is found for the two densest ridge spacings $S = \delta$ and $S = 0.5\delta$. However, for $S = 2\delta$ the spectra reveal contributions of VLSM at large streamwise wavelengths λ_x and $\lambda_z \approx 2\delta$, which appear closer to the ridges in the spanwise direction than seen for larger S. The contribution of these structures ($\lambda_z \approx 2\delta$) occurs over a higher wall-normal range compared to the contributions for $S > 2\delta$ and is not connected to the wall. For this case the spanwise spacing $S = 2\delta$ corresponds to the spanwise wavelength of VLSM naturally occurring in the smooth wall case. This suggests that for this specific ridge spacing, the appearance of the low-speed streaks at the ridge location related to secondary motion allow the simultaneous formation of VLSM. Of particular interest for future analysis will be cases where secondary motions and very-large-scale motions can coexist to investigate their similarities and differences.

ACKNOWLEDGEMENT

This work was performed on the supercomputer ForHLR II and the storage facility LSDF funded by the Ministry of Science, Research and the Arts Baden-Württemberg and by the Federal Ministry of Education and Research. The funding through DFG project number 423710075 is greatly acknowledged.

REFERENCES

Bartholomew, P., Deskos, G., Frantz, R. A. S., Schuch, F. N., Lamballais, E. & Laizet, S. 2020 Xcompact3D: An open-source framework for solving turbulence problems on a Cartesian mesh. *SoftwareX* **12**, 100550.

Gautier, R., Laizet, S. & Lamballais, E. 2014 A DNS study of jet control with microjets using an immersed boundary method. *International Journal of Computational Fluid Dynamics* **28** (6-10), 393–410.

Hutchins, N. & Marusic, Ivan 2007 Evidence of very long meandering features in the logarithmic region of turbulent boundary layers. *Journal of Fluid Mechanics* **579**, 1–28.

Schäfer, K., Stroh, A., Forooghi, P. & Frohnapfel, B. 2022 Modelling spanwise heterogeneous roughness through a parametric forcing approach. *Journal of Fluid Mechanics* **930**.

Stroh, A., Schäfer, K., Forooghi, P. & Frohnapfel, B. 2020 Secondary flow and heat transfer in turbulent flow over streamwise ridges. *International Journal of Heat and Fluid Flow* **81**.

Vanderwel, C., Stroh, A., Kriegseis, J., Frohnapfel, B. & Ganapathisubramani, B. 2019 The instantaneous structure of secondary flows in turbulent boundary layers. *Journal of Fluid Mechanics* **862**, 845–870.

Wangsawijaya, D. D., Baidya, R., Chung, D., Marusic, I. & Hutchins, N. 2020 The effect of spanwise wavelength of surface heterogeneity on turbulent secondary flows. *Journal of Fluid Mechanics* **894**.

Wangsawijaya, D. D. & Hutchins, N. 2022 Investigation of unsteady secondary flows and large-scale turbulence in heterogeneous turbulent boundary layers. *Journal of Fluid Mechanics* **934**, publisher: Cambridge University Press.

Zampiron, A., Cameron, S. & Nikora, V. 2020 Secondary currents and very-large-scale motions in open-channel flow over streamwise ridges. *Journal of Fluid Mechanics* **887**, A17.